2011

Magnetic Properties of the Bishop Ash in the San Andreas Fault Borderlands

Becky Strauss
Oberlin College

MAGNETIC PROPERTIES OF THE BISHOP ASH IN THE SAN ANDREAS FAULT BORDERLANDS

Becky Strauss

Honors Thesis, 2011

Oberlin College Department of Geology

ABSTRACT

The San Andreas Fault marks one of the most tectonically active regions of the United States, producing frequent earthquakes that have decimated major population centers throughout central and southern California. Its northern regions have been thoroughly studied, but the complex behavior of the southeast portion of the fault is often neglected, in spite of its potential to nucleate a major earthquake within the next few centuries. In this study, I examined the magnetic traits of the Bishop Ash, a well-dated marker horizon of volcanic ash, to assess deformation adjacent to this part of the fault at hand-sample scale. To this end, I first characterized the magnetic properties of the Ash and found that while magnetite is present in small concentrations, the anisotropy of magnetic susceptibility (AMS) is controlled by the crystallographic fabric of paramagnetic minerals. The scatter of anisotropy axes implies that individual grains may have been slightly reoriented during deformation. I also attempted to use magnetic remanence to determine whether significant vertical axis reorientation has occurred since initial deposition; however, the recorded remanence is likely a chemical remanent magnetization (CRM) acquired after deposition.

INTRODUCTION

The San Andreas fault zone is an active plate boundary that crosses central and southern California, a region rich with major population centers (Fig. 1). The fault extends from Cape Mendocino in the

northwest to the Imperial Valley in the southeast, incorporating the primary San Andreas Fault as well as multiple subsidiary faults. The trace of this fault system marks the boundary between the North American Plate to the east and the Pacific Plate to the west (Moores & Twiss, 1995). Due to its proximity to multiple major cities, the San Andreas Fault has been extensively studied at a variety of scales in order to describe its motion and characterize future seismic events. Though it is classified as a right-lateral strike-slip fault delineating a transform plate boundary, variations in the geometry and movement of the plates produce localized regions of shortening across the fault, which in turn gives rise to a combination of wrench motion and convergence.

Figure 1. Map of the trace of the San Andreas Fault (in red), which passes near major cities in California. Study area is located in boxed region; see Appendix B for satellite image. (Modified from French, 2006)

The seismic hazards associated with the northern segments of the San Andreas Fault are well known, having generated sizeable earthquakes near major cities including San Francisco in 1906 and Santa Cruz and San Jose in 1985. However, the southernmost portion of the fault, known as the Coachella or Indio segment, has only recently been subject to thorough study. The Coachella segment, which has not experienced a major earthquake since the 17th century, seems relatively inactive compared to the northern segments. Bürgmann (1991) pointed out that the region exhibits high rates of strain, only about 10% of which is accommodated by the creep rate of the fault. He suggested that since the last historic earthquake along the Coachella segment, 6 to 9 meters of slip deficit have accumulated. Sykes and Nishenko (1984) estimated a future earthquake with a magnitude of 7.7 and a recurrence interval of 160-360 years, from which Bürgmann (1991) inferred a high earthquake hazard in the region. Philibosian et al. (2011) estimated an average recurrence interval of 180 years, similarly inferring that the Coachella segment has accumulated a large amount of tectonic stress that may result in a major quake in the near future. Johnson and Hutton (1982, 1986) suggested that a quake of this

magnitude may originate from a point of concentrated loading on the southernmost SAF. Bürgmann (1991) proposed the location of such a point at Durmid Hill.

To calculate a slip deficit in the San Andreas fault zone, we must evaluate the partitioning of relative plate motion between slip on the main trace of the San Andreas Fault, slip on sub-parallel faults, and accommodation by deformation of the borderlands. Compilations of slip rates on faults on southern California (e.g. Agnew et al., 2002) show that slip on both the San Jacinto and Elsinore faults accommodate some of the plate motion; the remainder must be either stored elastically, hence the slip deficit, or accommodated by distortion distributed across the rock masses between the faults. This study of the magnetic properties of the Bishop Ash is intended to contribute to our assessment of the magnitude of deformation in the borderlands of the fault.

GEOLOGIC SETTING

Durmid Hill is a geomorphological feature located between the Salton Sea and the San Andreas Fault. Its topographic expression is a low, elongate dome 20 km long and 4 km wide, with a maximum height of 30 m above sea level, 107 m above the 1985 level of the Salton Sea. Beneath surface deposits of mud and sand deposited by Lake Cahuilla, the predecessor of the Salton Sea, Plio-Pleistocene sandstone and siltstone beds dip away from the fault (Sylvester, 1993). Babcock (1974) called this subsurface structure the "Durmid anticline", a doubly plunging anticline with tightly compressed folds on its southwest limb and no apparent northeast limb. Bürgmann (1991) examined map-scale deformation to offer transpression as an alternate model. His analysis of the Bishop Ash, a lacustrine bed in the Pleistocene Brawley Formation, provides a key to unraveling the complex subsurface structure. (Bürgmann used the existing stratigraphic correlations to place these units in the Borrego Formation; see Lutz and others (2006; GSA Bulletin) for a reassignment of these units to the Brawley Formation.)

The Bishop Ash (Fig. 2), first recognized at Durmid Hill by Babcock (1974), is a well-dated marker horizon of volcanic ash found throughout the southwestern United States, covering an area of greater than 2 million km^2. It was produced and deposited concurrently with the Bishop Tuff in the eruption that formed the Long Valley

Figure 2. Photo of the surface trace of the Bishop Ash at Durmid Hill.

Caldera, located in eastern California. The Bishop Ash was most recently dated to 758.9 ± 1.8 kya, soon after the Matuyama Reversed-Brunhes Normal (M-B) paleomagnetic transition 774.8 ± 2.8 kya (Sarna-Wojcicki, 2000). At Durmid Hill, the ash layer was subsequently buried beneath 500-1000 m of sediment (Wojtal, personal communication, 2011). Due to its huge extent and well-dated isochronous deposition, this rhyolitic ash bed is a key chronostratigraphic marker for the region.

By tracking the system of thrust and extensional faults, folds, and boudinage in the Bishop Ash, Bürgmann (1991) demonstrated that the Brawley Formation adjacent to the San Andreas Fault experienced significant uplift, accompanied by shortening perpendicular to the fault and lengthening parallel to the fault (Fig. 3). Durmid Hill therefore follows the transpressional model suggested by Harland (1971), whereby shortening across a zone in which no volume change takes place is compensated for by vertical thickening. Sylvester (1993) measured an uplift of 1.5 mm/year, which fits Bürgmann's calculated uplift of 1.1-1.7 mm/year and supports the inference of transpression along this segment of the fault.
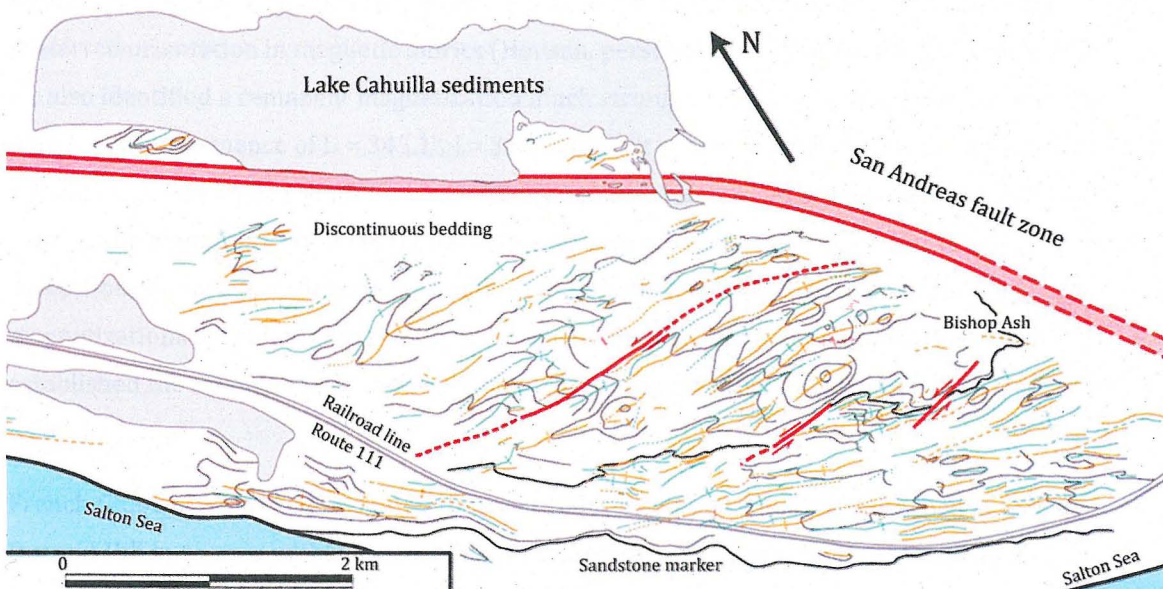
Figure 3. Map of the Bishop Ash at Durmid Hill, modified from Bürgmann (1991) and Babcock (1974). Red lines indicate fault traces; green and yellow lines mark synclines and anticlines respectively. (via Wojtal)

ROCK MAGNETISM AND THE BISHOP ASH

Due to the fine grain sizes and friability of the Bishop Ash, hand- and microscopic-scale deformation is difficult, if not impossible, to determine through optical techniques. Rock magnetism provides an alternative set of methods, enabling the analysis of such samples according to their magnetic behavior. Magnetization, M, is defined as the magnetic dipole moment per unit volume that results

5

when a solid sample is placed in a magnetic field of known strength, H. Its response to applied fields and variations of temperature may be measured in samples whose grains are too small to study optically. (See Appendix A for a chart of variables used in this paper.)

Variation in the response of M when fields are applied at different orientations may be measured and interpreted in terms of grain shape and crystalline alignment (Tarling & Hrouda, 1993). Anisotropy of magnetic susceptibility (AMS) quantifies this variation by measuring the directional dependence of induced magnetization. The resulting vectors describe the sample's susceptibility, a dimensionless quantity representing the ease with which magnetization changes in response to an applied field.

Lutz, Dorsey, Housen, & Janecke (2006) studied fault-controlled sedimentation in the Borrego Badlands near Anza-Borrego, an area to the southwest of the Salton Sea. This region lies on the San Jacinto fault zone, about 30 km west of the main San Andreas Fault. Though the results were not published, Housen examined the AMS of the Bishop Ash in the Borrego Badlands, finding a preferred orientation in magnetic fabrics (Housen, personal communication with French, 2006). He also identified a remanent magnetization much stronger than that measured at Durmid Hill, with a mean remanence of D = 345.1°, I = 38.6° after tilt correction, where D is the declination from north and I is the inclination from horizontal (Housen, personal communication, 2011). Related work in the overlying Ocotillo Formation showed a mean remanence of D = 360°, I = 38.2° after tilt correction, giving a post-deposition rotation of <8° with 95% confidence (Lutz, 2006). Measured magnetizations at this site were tightly clustered with consistent orientations. (Palmer (1996) established the original orientation of the remanent magnetism of the Bishop Tuff as D = ~348°, I = ~53° .)

French (2006) and French, Wojtal, & Housen (2006) examined the AMS of the Bishop Ash at Durmid Hill in an area within 1 km of the San Andreas Fault, where significant near-fault deformation is readily apparent at map scale. For instance, outcrops of the Bishop Ash farther than 1 km from the main fault are 1.5-2 m thick; in contrast, those within 1 km of the fault range from 1 m thick at the hinge of Babcock's "Durmid anticline" to less than 50 cm as the layer strikes into the fault (Wojtal, 2008, 2009). In this region, the Ash exhibits an AMS fabric unlike that of exposures far from the fault, which can be readily correlated to depositional layering in the Ash. Rather, the study by French (2006) found that samples from Durmid exhibit an irregular orientation, generally oblique to the depositional layering in these rocks, which indicates that they have likely experienced deformation at the scale of hand samples. In some samples, magnetic fabrics show a

regular orientation relative to fold hinges and cleavage, consistent with the working model of transpression at Durmid Hill.

Wojtal (2008, 2009) documented lateral gradients in the amount of deformation accommodated by folding and minor faulting at varying distances from the San Andreas Fault, finding the greatest intensity of deformation near the main fault and decreasing intensity with distance from the fault. This deformation gradient is consistent with the results of Bürgmann's (1991) study of the orientations of fold hinges. Wojtal observed that at distances greater than 1 km from the main fault, the Bishop Ash is still tightly folded and, due to elongation parallel to fold hinges, often crops out as blunt-ended boudins. Based on the work of French (2006), it was suggested that a lateral gradient in deformation magnitude could be quantified through AMS measurements.

While the study by French (2006) documented the effects of deformation near the San Andreas Fault, the number of samples analyzed and the results of this analysis left room for further study. French inferred from the presence of remanent magnetism that the Bishop Ash must include some ferromagnetic component (Housen, personal communication with French, 2006). However, the small size and low concentration of ferromagnetic minerals in most sedimentary rocks makes identification through optical and scanning microscopy notoriously difficult. (Butler, 1992) French (2006) was unable to find such minerals through these methods, though she documented the presence of feldspars and amphiboles. These results are consistent with Anderson (2000), who reported the major element compositions of matrix glasses as 77.5 wt % SiO_2, 12.7 wt % Al_2O_3, 3.5 wt % Na_2O, and 4.96 to 5.49 wt % K_2O. In French's XRF analysis, the Bishop Ash from Durmid Hill showed slight loss of silica, sodium, and potassium, as well as iron enrichment, when compared to unaltered samples from a different location (French, 2006). If this comparison is valid, it implies that the Durmid Hill samples have been slightly altered since initial deposition, consistent with Anderson's proposal that the alkalis in this matrix may have been affected by leaching or weathering (French, 2006; Anderson, 2000).

In this study, I apply rock magnetic techniques to address the questions posed by French (2006) and identify the magnetic carriers in the Bishop Ash at Durmid Hill. I also expand the study area addressed in previous AMS work, filling the geographic gap between French (2006) and Lutz (2006) by focusing upon a group of samples collected in an area 1-3 km to the west of the San Andreas Fault, adjacent to the Salton Sea. Further, I attempt to determine the extent of vertical axis reorientation in this area by measuring remanent magnetization and comparing it to the results of

Palmer (1996) and Lutz (2006). These three approaches use rock magnetism to expand upon our understanding of the Bishop Ash and its interaction with the San Andreas Fault.

METHODS

FIELD WORK

Samples from the Durmid Hill region were collected by Dr. Steven Wojtal during June and July 2007. The sample area is located on a 3 km-wide strip of desert between the San Andreas Fault and the Salton Sea. Samples were taken from exposed traces of the Bishop Ash spanning an area about 5 km long, oriented oblique to the fault in a zone 1-3 km to its west. This region was selected to fill in a physical gap between previous studies, which had analyzed deformation within 1 km of the fault (French 2006) and on the opposite side of the Salton Sea (Lutz 2006).

SAMPLING

The Bishop Ash at Durmid Hill is well exposed in straight-walled channels 1-2 m deep, often extending up to 50 cm above the base elevation in the relatively flat expanses or narrow ribs separating the channels (Fig. 4). These channels are most likely the products of flash flooding, inferred from the general lack of rainfall in the region and the presence of debris flows. Most of the samples were taken from easily accessible channel profiles, while a few were collected from the tops of ribs between channels. (See Appendix B for a map of sample source locations.)

Figure 4. Photo of the Bishop Ash (lightest layers dipping to the right) exposed in the wall of a channel.

Dr. Wojtal used a hacksaw to define the edges of each sample and then chiseled it free from the outcrop. As samples were collected, they were oriented by their top surfaces: either natural bedding surfaces or smooth surfaces scraped with a knife before removal from the outcrop. Strikes and dips were measured on-site and marked on these surfaces.

Sample selection was primarily dictated by the friability of the Bishop Ash. Only samples coherent enough to maintain appreciable size were collected. Dr. Wojtal also considered each sample's robustness during collection, as samples had to be transported cross-country prior to epoxy impregnation. The resulting set was 27 hand samples, one of which was discarded due to structural collapse upon return to Oberlin, leaving 26 samples for study.

LABORATORY METHODS

In preparation for magnetic measurements, I sawed each of the 26 hand samples into 2 cm³ cubes oriented relative to their marked strikes and dips. After each cut, I covered the newly exposed surface with a thin veneer of epoxy to prevent further crumbling. Where possible, hand samples produced four usable cubes; several samples were large and coherent enough to produce five. A few of the more friable samples yielded only three cubes before falling apart. A total of 117 cubes were produced, though nine did not retain coherence, leaving 108 usable cubes.

Laboratory work was conducted in January 2011 at the University of Minnesota's Institute for Rock Magnetism (IRM). This research was made possible by a U.S. Visiting Student Fellowship from the IRM.

Three samples were also studied in thin section through petrographic and scanning electron microscopy (SEM) at Oberlin College. I used a JEOL SEM, model JSM-5610LV, at 20 kV with a working distance of 15 mm and spot sizes of 24 and 32. Two samples, one finer-grained and one coarser-grained, were chosen from adjacent sites at the eastern end of the study area, closest to the San Andreas Fault. The third sample was randomly selected from the middle region of the study area with the intent of comparing the extent of deformation between sample sites. Thin sections were taken perpendicular to bedding.
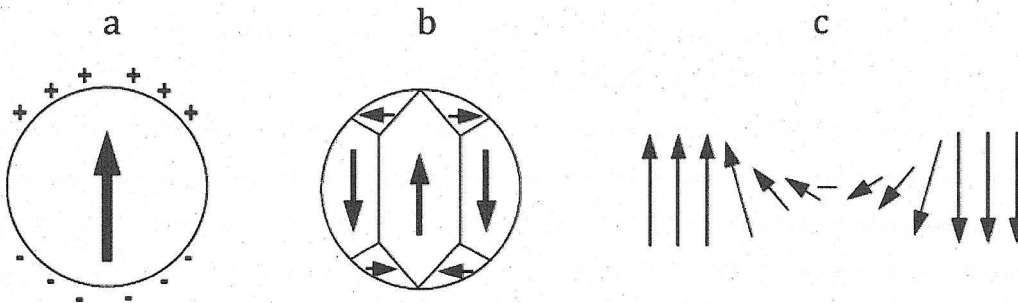
MAGNETIC CHARACTERIZATION

Magnetic characterization is the determination of a sample's unique magnetic traits from its response to varying temperature and applied field conditions. Through these traits, including domain states and overall magnetic behavior, we can categorize the concentrations, compositions, and particle size distributions of magnetic minerals. To determine these properties, I used two complementary instruments: a Magnetic Property Measurement System (MPMS) and a Vibrating Sample Magnetometer (VSM).

Domain States and Grain Size (via Butler, 1992)

Atomic magnetic moments may be modeled as pairs of positive and negative magnetic charges. The charges of adjacent atoms cancel out within a given ferromagnetic particle; however, a magnetic charge distribution is produced at the particle's surface. In a small, spherical particle, one hemisphere has positive charge, while the other has negative charge (Fig. 5a). Due to the repulsion between adjacent charges, magnetostatic energy is stored in this charge distribution.

The optimal state for any grain is that of the lowest magnetostatic energy. To reduce this energy, *magnetic domains* compartmentalize a grain's magnetic charges so that opposite charges are adjacent (Fig. 5b). Domains are separated by *domain walls*, regions in which exchange energy between adjacent atoms causes the orientation of atomic magnetic moments to rotate (Fig. 5c). The number of domains present within a grain increases with its size.

Figure 5. (a) Uniformly magnetized sphere of ferromagnetic material with hemispheric charge distribution; arrow indicates the direction of saturation magnetization, M_s, the maximum quantity beyond which magnetization will not increase regardless of further increase in applied field strength, H. (b) Sphere of ferromagnetic material subdivided into magnetic domains; arrows show the directions of M_s within individual magnetic domains, separated by planar domain walls. (c) Rotation of magnetic moments within a domain wall; arrows represent atomic magnetic moments which spiral inside the domain wall. (Butler, 1992)

Single-domain (SD) grains are so small that the energy required to produce a domain wall is greater than the decrease in magnetostatic energy that would result. Each ferromagnetic mineral has a unique diameter below which grains are SD, termed the "single-domain threshold grain size" (Butler, 1992) or the "critical single-domain size" (Dunlop & Özdemir, 1997). *Multi-domain (MD)* grains, which are substantially larger than SD grains, contain many domains separated by domain walls. A sample's domain state may be determined through the analysis of its magnetic properties, enabling the calculation of a probable grain size range.

The ***Magnetic Property Measurement System (MPMS)*** imparts an isothermal remanent magnetization (IRM) to a sample by briefly applying a strong field at a constant temperature, after which it measures the behavior of this IRM with changing temperature and the presence or absence

11

of an applied magnetic field. This instrument may be programmed to run complex sequences of measurements, with a temperature range of 2.1 K to 300 K and the application of fields up to 5 T.

I used two sequences: *Run A*, a thorough sequence that ran for twenty hours overnight, and *Run B*, a simpler sequence that ran for three hours. Due to the associated time restraints, I selected three samples for *Run A* and two for *Run B*. These five samples were randomly chosen from a range of source locations and represented a variety of grain sizes. The properties measured by the MPMS are independent of orientation, so I ground a piece of each sample into grains, which were then inserted into a medical gel cap sealed with heat-resistant tape and suspended in a drinking straw. The straw was attached to the end of a metal rod and lowered into the vacuum-sealed body of the MPMS.

The long sequence, *Run A*, involved two components. The first segment of the sequence was an *FC-ZFC (field cool-zero field cool) experiment*. The sample was cooled in a field of 2.5 T to 10 K, where a 2.5 T IRM was imparted. With the field off, remanence was measured on warming to 300 K. The sample was then cooled to 10 K again, this time in zero field, and given a 2.5 T IRM. Again, remanence was measured on warming to 300 K. This dual process enables the comparison of FC and ZFC remanence to determine the sample's domain state, a measure of the size-dependent magnetic charge distribution at a given particle's surface. The second portion of the sequence was *the low-temperature cycling of a room-temperature IRM*. A 2.5 T IRM was imparted at 300 K; remanence and susceptibility were measured during cooling to 10 K and then during warming to 300 K, both in zero field. The characteristic responses of certain minerals and grain size distributions to such variation are diagnostic of their presence in a sample. For instance, minerals such as magnetite and hematite undergo distinctive mineralogical transitions at 120 K and 50 K respectively; this property allows for unambiguous quantitative identification.

The short sequence, *Run B*, was conducted entirely in zero field. A 2.5 T IRM was imparted at 300 K; remanence was measured during cooling to 20 K. A 2.5 T IRM was again imparted at 20 K; remanence was measured during warming to 300 K.

(Note: "Zero field" here refers to the near-zero-field environment, valid to within 1-2 μT, created within the MPMS along the measurement axis.)

The **Vibrating Sample Magnetometer (VSM)** measures the response of a sample's magnetization, *M*, to an applied magnetic field, *H*, of changing intensity and direction. *H* increases to a given magnitude in the positive direction, decreases to zero, reverses direction, increases to the same

magnitude, and decreases to zero again. This cycle is repeated multiple times for greater accuracy of measurement.

Three main categories of magnetic behavior, distinguished by the response of M to changes in H, may be observed: diamagnetism, paramagnetism, and ferromagnetism. In diamagnetic materials, an applied field, H, induces a small magnetization, M, in the opposite direction; this magnetization has a linear dependence upon the applied field (Fig. 6a). Upon removal of the field, the induced magnetization drops to zero. In paramagnetic materials, a small magnetization, M, is induced parallel to the applied field, H; again, the magnetization is linearly dependent upon the applied field (Fig. 6b). When the field is removed, magnetization drops to zero.
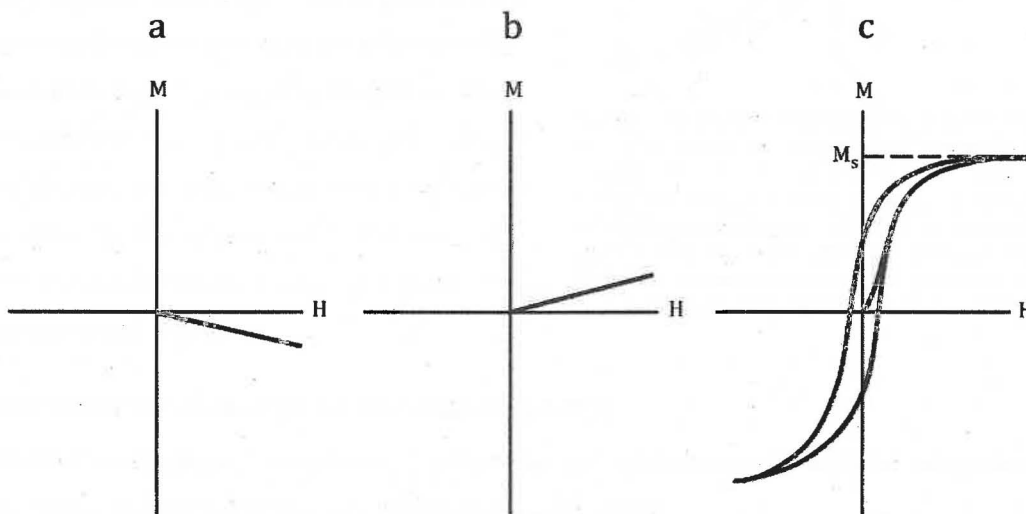
Figure 6. (a) Magnetization, M, versus magnetizing field, H, for a diamagnetic material. (b) M versus H for a paramagnetic material. (c) M versus H for a ferromagnetic substance; the path of magnetization exhibits hysteresis and the relationship between M and H is not a simple constant. (Butler, 1992)

In ferromagnetic materials, unlike paramagnetic and diamagnetic materials, the magnetic moments of adjacent atoms align and interact strongly. As a result, the application of a magnetic field, H, induces a magnetization, M, several orders of magnitude larger than that induced in paramagnetic materials by the same field. As this field is removed, M does not automatically return to zero; rather, it retains a record of the field, following an irreversible path in response to the change in H (Fig. 6c). This path, produced when M is plotted as a function of H, is a *hysteresis loop* (Fig. 7). (Butler, 1992)

For each ferromagnetic material, there exists a maximum quantity, M_s, beyond which magnetization will not increase, regardless of further increase in H. This quantity, called the *saturation magnetization*, is the highest magnetization in the material's hysteresis loop (Fig. 7.2). When H is removed, a *saturation remanent magnetization*, M_r, remains (Fig. 7.3). The intensity of the reverse field required to reduce M all the way back to zero is the *coercive force* or *coercivity*, H_c. (Butler, 1992;, Dunlop & Özdemir, 1997)

I used a room-temperature VSM to generate hysteresis loops for five samples, four of which had already been measured in the MPMS. The fifth sample was arbitrarily chosen when extra time became available. A cube from each sample was affixed to the sample holder with masking tape. Measurements were taken at constant room temperature of 300 K.
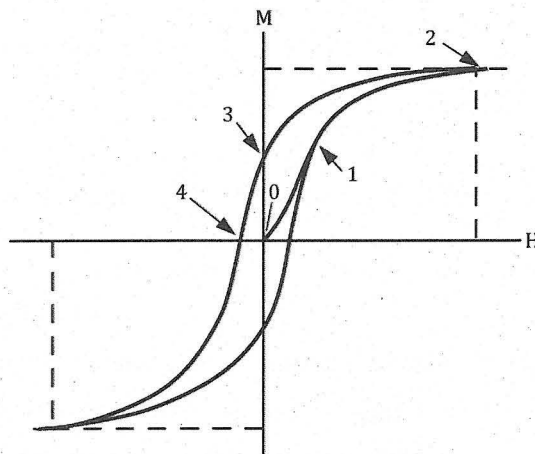
Figure 7. Hysteresis loop for a synthetic sample containing 5% by volume of dispersed elongated single-domain (SD) magnetite particles. At point 1, the magnetization of each grain is rotating to align with the applied field H. At point 2, the sample is at saturation magnetization M_s. At point 3, the magnetizing field has been removed, magnetizations are rotating away from H, and the sample is at saturation remanent magnetization M_r. At point 4, magnetization has returned to zero. (Butler, 1992)

ANISOTROPY OF MAGNETIC SUSCEPTIBILITY (AMS)

Anisotropy of Magnetic Susceptibility (AMS) measures the anisotropy of induced magnetization to determine a sample's directionally dependent susceptibility.

When a rock specimen is placed in a magnetic field of known intensity, H, the resulting magnetization, M, may be used to determine K, the susceptibility per unit volume.

$$M = KH \rightarrow K = M/H$$

In some rocks, M will always have the same strength, regardless of the direction in which the field H is applied. The susceptibility in this instance is the same in all directions and K acts as a proportionality constant. Such rocks are magnetically isotropic.

In most rocks, however, the value of M depends upon the orientation of the sample in the field. These rocks are magnetically anisotropic. When a low field (<1 mT) is applied to a magnetically anisotropic specimen, the induced magnetization, M, does not have the same magnitude in all directions. The relationship between M and H is defined by three orthogonal components

representing the sample's directional susceptibility. Their relationship is most easily visualized as an ellipsoid with three principal axes, K_{max}, K_{int}, and K_{min}, where K_{max} is the axis with the greatest magnitude of susceptibility, K_{min} is that with the smallest magnitude, and K_{int} is the intermediary (Fig. 8). Anisotropy is controlled by the combined orientation distribution of all minerals in the specimen. (Tarling & Hrouda, 1993; Borradaile & Jackson, 2004)
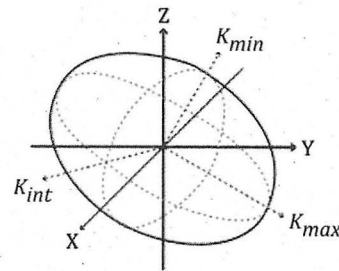
Figure 8. The susceptibility ellipsoid is defined by three principal axes, K_{max}, K_{int}, and K_{min}. (Tarling & Hrouda, 1993; French, 2006)

The *Kappabridge* is a modified AC bridge that measures the directional susceptibility of a sample along a minimum of six directions to enable the construction of a susceptibility ellipsoid. One arm of the AC bridge is an inductive coil; when a sample is inserted, the change in inductance in the coil is proportional to the sample's susceptibility.

Sample cubes were placed in a plastic holder, which was rotated by hand and inserted into the instrument with fifteen different orientations to produce a total of fifteen measurements. Repetition of measurement was included to allow the estimation of errors.

Due to sample friability and the resulting abundance of loose grains, all parts of the holder were wiped down with an isopropyl alcohol solution before each set of measurements.

REMANENCE

Remanence is used to describe a sample's paleomagnetic orientation, providing insight on positional changes that may have occurred since acquisition of this magnetic signal. When rocks are magnetized in situ, their magnetization, M, is the vector sum of two components: the induced magnetization, M_i, and the natural remanent magnetization, M_r.

$$M = M_i + M_r$$

The induced magnetization, M_i, is a function of the local geomagnetic field, H, which acts as the applied field, and the sample's mass-normalized bulk susceptibility, χ.

$$M_i = \chi H$$

Natural remanent magnetization (NRM) is the remanent magnetization that is naturally preserved in a rock before alteration in a laboratory environment. NRM is typically the vector sum of two components:

15

NRM = primary NRM + secondary NRM

Primary NRM is the component acquired during rock formation that records the ambient geomagnetic field. Its common forms include thermoremanent magnetization (TRM), which is acquired when a rock cools through its Curie temperature; chemical remanent magnetization (CRM), which is produced by the growth of ferromagnetic grains below the Curie temperature; and detrital remanent magnetization (DRM), which results from the accumulation of sedimentary rocks containing detrital ferromagnetic minerals.

Secondary NRM is acquired after rock formation as a result of processes including the viscous decay of magnetization over time, chemical alteration and growth of magnetic minerals, or lightning strikes. These processes may alter or obscure the primary NRM, which most studies intend to measure. (Butler, 1992; Merrill et al., 1996)

Measurements were collected using a 2G Enterprises *SQUID (Superconducting QUantum Interference Device) Magnetometer*. SQUID magnetometers are distinguished by their high sensitivity and fast response times, eliminating the need for vibration or spinning of samples as with earlier instruments. When a sample is inserted into the magnetometer's superconducting sense coils, which are arranged in three orthogonal sets, a DC persistent current is induced. The induced current gives a field at the SQUID sensor via a flux transformer. The sensor detects this field as a measure of the sample's magnetization along three orthogonal axes, describing the magnetization as a three-dimensional vector. (Goree & Fuller, 1976; Feinberg, personal communication, 2011)

The sense coils, transformer, and detector are housed in a superconducting shield, which eliminates the effects of fluctuations in the geomagnetic field (Goree & Fuller, 1976). In addition, the SQUID magnetometer at the IRM is located in a shielded room, whose two layers of transformer steel attenuate the background magnetic field to <1 µT (Bowles, 2008). (The modern geomagnetic field strength is about 30-60 µT.) In weak samples, repeatability of results is determined by proximity to the noise level of the instrument. The 2G Enterprises SQUID at the IRM has a sensitivity of $\sim 2 \times 10^{-12}$ Am^2.

The 2G Enterprises SQUID that I used is equipped to measure long cores or groups of up to eight discrete samples at a time. Samples are attached at regular intervals to a computer-controlled holder tray with masking tape. To measure the characteristic remanent magnetization (ChRM) of my samples, I used an alternating field (AF) demagnetization sequence, one of several progressive

demagnetization techniques intended to separate and reduce the effects of secondary NRM and post-collection contamination. AF demagnetization exposes samples to alternating magnetic fields of linearly decreasing magnitude, forcing the directional switching of magnetic moments that cancel out to erase the NRM carried by grains with coercivities less than the field magnitude (Butler, 1992). This technique is often effective in removing secondary NRM in order to isolate ChRM, though it may not clear up viscous contamination as well as thermal demagnetization methods (Goree & Fuller, 1976).

I measured the ChRM of 46 cubes from 12 different samples, taken from sites throughout the study area. Due to instrument capacity and timing constraints, one to two samples were randomly selected from each cluster of sampling locations in the eastern half of the study area, in addition to cubes from all but one of the sample sites in the less tightly distributed zone to the west. Three of the selected samples only had three usable cubes, eight samples had four cubes, and one sample had five. The resulting declinations and inclinations were plotted with Richard Allmendinger and Néstor Cardozo's OSXStereonet (available at http://homepage.mac.com/nfcd/work/programs.html) and rotated with bedding to horizontal for analysis.

RESULTS

CHARACTERIZATION

MPMS

(Note: The two components of this experiment are described in reverse order for clarity of explanation.)

The second component of *Run A*, the low-temperature cycling of a room-temperature IRM, is broken down into AC and DC portions. *Run B* performed the same experiments as the DC portion of *Run A*.

AC:

The relationship between applied field strength, H, and the resulting induced magnetization, M, is described by the mass-normalized bulk susceptibility, χ:

$$M = \chi H$$

During the low-temperature cycling experiment, susceptibility was measured in relation to changing temperature, T. In all three samples, susceptibility exhibits a $1/T$ decrease with increasing temperature (Fig. 9). This relationship behaves according to the Curie Law of paramagnetic susceptibility, which quantifies the response of paramagnetic materials to temperature change.

In paramagnetic materials, the thermal energy of temperatures above absolute zero vibrates the crystal lattice, thereby triggering rapid, random oscillation of atomic magnetic moment orientations, which results in a low susceptibility. As the temperature decreases, so do the effects of thermal energy; at low temperatures,

Figure 9. Susceptibility, χ, vs. temperature, T, in sample 07001. All samples measured showed the same trend.

moments align to produce a significantly higher susceptibility. This relationship is encompassed in the Curie Law, expressed as the equation

18

$$M = \chi * H = C * (H/T)$$

where M = magnetization, χ = susceptibility, H = applied field strength, and C = a material-specific Curie constant (Butler, 1992; Feinberg, personal communication, 2011). The magnetization of these ash samples must therefore be dominated by contributions from paramagnetic minerals.

Superparamagnetic grains, which are even smaller than SD (single-domain) grains and tend to retain magnetization for between a fraction of a second and two minutes, exhibit frequency dependence when exposed to an alternating current. Susceptibility, χ, acts as an indicator of a grain's ability to follow the frequency of alternation. In these samples, the susceptibility shows no frequency dependence, indicating that there are no grains of superparamagnetic size in these samples. (Butler, 1992; Feinberg, personal communication, 2011)

DC:

Magnetization, M, was measured with respect to temperature, T, as part of the low-temperature cycling experiment. In both runs and all five samples, an abrupt decrease in magnetization and a shift in room temperature (RT) remanence occurred at 120 K (Fig. 10). This sudden change was identified as the Verwey transition, a phase transition exclusive to magnetite.

When stoichiometric magnetite (Fe_3O_4) is cooled past 120 K, it undergoes a first-order phase transition from cubic to monoclinic symmetry. Above 120 K, electrons hop from Fe^{2+} to Fe^{3+}, converting the Fe^{2+} to Fe^{3+} and vice versa in a disordered arrangement. Below 120 K, electron hopping stops; there is an ordered arrangement of Fe^{2+} and Fe^{3+} ions, which

Figure 10. Magnetization, M, vs. temperature, T, in sample 07002. The black line represents RT remanence on cooling; the green line represents RT remanence on warming. As the temperature cools past 120 K, magnetization drops sharply. All samples measured showed similar trends.

induces the distortion of the unit cell lattice. This change in magnetocrystalline anisotropy produces a sudden drop in magnetization known as the Verwey transition (Tauxe, 2005; Dunlop & Özdemir, 1997; and others).

A similar diagnostic transition exists for hematite, which experiences a change in magnetization at 250 K. This change, known as the Morin transition, did not occur in any of my measured samples, from which I infer the absence of hematite.

The first component of *Run A*, the FC-ZFC experiment, was intended to enable the comparison of FC and ZFC remanence to determine the sample's domain state. In an SD grain, interior magnetization is uniform, so the grain's entire volume contributes toward its net magnetization. A sample dominated by SD grains would exhibit magnetization strongly aligned with the applied field in an FC experiment, while in a ZFC experiment its grain magnetizations would be randomly oriented, resulting in a much weaker net magnetization. In an MD grain, the opposing orientations of adjacent domains cancel out, so only a small fraction of the grain contributes to its net magnetization. Thus, a sample dominated by MD grains would exhibit a weak net magnetization in both FC and ZFC experiments, as its magnetization would only align weakly with the applied field in FC.
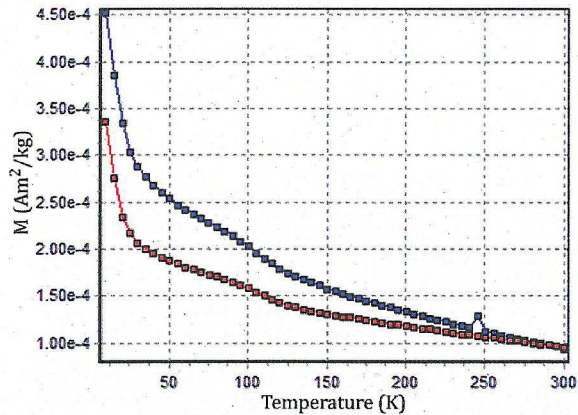
Figure 11. Magnetization, *M*, vs. temperature, *T*, in sample 07002. The blue line shows FC data, while the red line shows ZFC data. All samples measured showed the same trend.

All three samples processed through *Run A* showed a higher magnetization at cooler temperatures in FC than in ZFC, indicating that a significant portion of the assemblage is comprised of single-domain (SD) grains (Fig. 11). The ferromagnetic component of magnetization is therefore produced by SD magnetite.

VSM

The hysteresis loops produced for all five samples exhibit a dominantly paramagnetic signal with magnetization, *M*, parallel to the applied field, *H*. A very small ferromagnetic component was also detected (Fig. 12). These findings confirm the results from the MPMS.
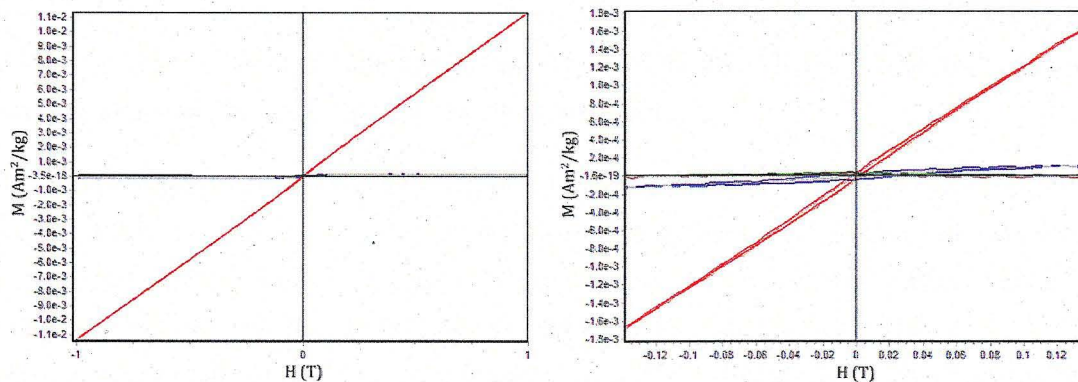
Figure 12. Hysteresis loops (*M* vs. *H*) from sample 07001. The red line indicates the magnetization path. *Left:* full hysteresis loop dominated by paramagnetism. *Right:* zoomed in to show small ferromagnetic component. All measured samples exhibited similar trends.

PETROGRAPHIC AND SCANNING ELECTRON MICROSCOPY (SEM)

A petrographic microscope was used for preliminary analysis of thin sections from three samples, two of which were also studied via SEM. All three thin sections are comprised mainly of glass whose composition is dominated by silica with small potassium and sodium contributions.

Sample 07002, the coarsest-grained of the three samples studied, has a mean grain size of around 100 μm. These grains are as coarse ash, which would be classified as fine sand according to the Udden-Wentworth size grade scale. Ash grains are primarily shards, including many tricuspate shapes (Fig. 13), and a few contain intact bubbles (Fig. 14). Fragments of pumice and tube pumice comparable in size to the shards are also scattered throughout the section.
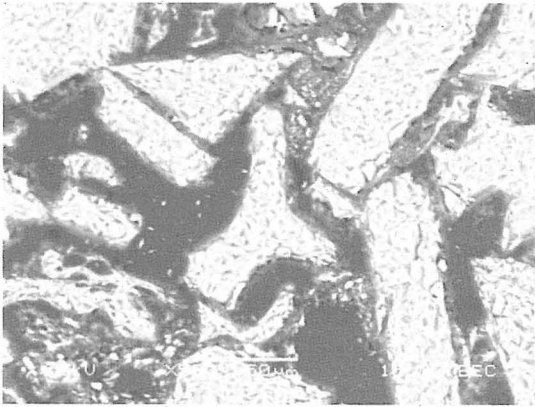
Figure 13. BSE image of tricuspate ash shard in sample 07002. Scale bar is 50 μm.
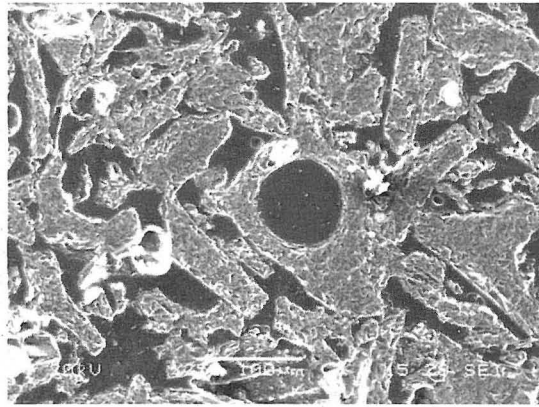
Figure 14. BSE image of intact bubble in sample 07002. Scale bar is 100μm.

Mineral grains, such as subhedral feldspars and biotites, are in the minority. Biotite grains are oriented roughly parallel to bedding and to each other; elongate ash grains also show some degree of preferential orientation parallel to bedding, though there is substantial scatter. The glass shards in this thin section have very thin coatings made visible between crossed polarizers by their length-slow alignment parallel to the shard edges. These coatings are more prominent around some grains than others. Similar coatings do not appear inside the intact bubbles; thus, the coatings must have accumulated at some point after initial ash formation.

Samples 07001 and 07025 are much finer-grained than sample 07002; both consist of fine ash, comparable to medium silt on the Udden-Wentworth size grade scale. Sample 07001 has a mean grain size of about 15 μm, while sample 07025 has a mean grain size of about 50 μm. In both samples, ash grains have been broken into smaller chip-like fragments with relatively equidimensional shapes (Fig. 15). Comparably sized crystals of biotite and feldspar are randomly scattered throughout the sections. Sample 07025 is thinly laminated with millimeter-scale bands of

varying grain size, some of which show normal grading; thus, it is likely that these bands formed during multiple episodes of ash settling in still water or small density currents. Such bands are not apparent in sample 07001, which appears to be massively bedded. Neither fine-grained sample shows optical evidence of any coating on the particles, which are uniformly dark between crossed polarizers. This apparent lack 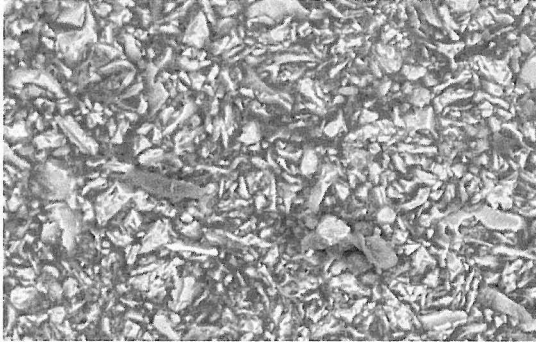of grain coatings in these samples may be a function of their lower permeabilities, which would restrict the throughput of pore water, thereby impeding all reasonable mechanisms for the formation of the coating, especially the precipitation of cement and the import of illuvial clay. Chemical alteration of the glass could be responsible for a clay coating, although the coating is not exclusive to the glass shards; some of the biotite crystals are similarly coated.

Figure 14. BSE image of ash grains in sample 07001. Darker grey shapes are grit on the thin section. Scale bar is 50 μm.

All three samples exhibit significant compaction, indicated by a lower porosity than would be anticipated in fresh, uncompacted lacustrine sediment. Many of the glass shards in sample 07002 are cracked, while biotite grains are bent or frayed (Fig. 16), with about three to five contacts per grain. Samples 07001 and 07025 show about six to eight contacts per grain. Additionally, there is a preferred orientation of elongate grains roughly parallel to bedding, though orientations at grain scale vary by about ±30° from parallel and there are multiple exceptions to this trend. Further study in more detail will be required to quantitatively assess the degree of grain alignment. There are no obvious optical signs of chemical alteration, though alteration may have occurred at an unobservable scale.
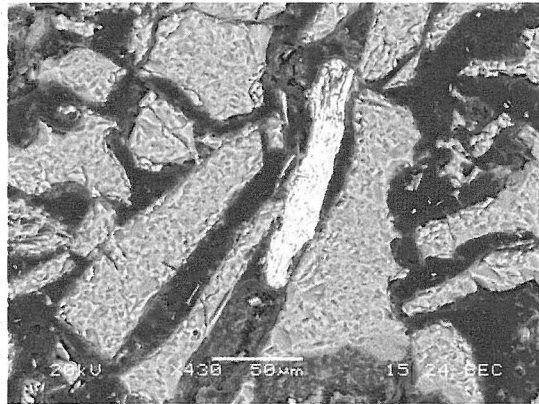
Figure 15. BSE image of biotite grain (center) with frayed end in sample 07002. Scale bar is 50μm.

As only three samples out of 26 were studied in thin section, it is not known to what extent to which these results are representative of the entire set of samples.

AMS

All 107 cubes measured in the Kappabridge exhibit extremely weak susceptibility and low anisotropy. The weakness of these susceptibility signals is a major contributor to the difficulty experienced in analyzing the data in a meaningful way.

The overall results of my AMS study are very similar to those of French (2006), implying that the magnetic traits of the Bishop Ash at Durmid Hill are geographically consistent across several kilometers. To describe these traits, I follow French's approach and plot shape factor, T, against mean susceptibility, K_M, and corrected degree of anisotropy, Pj.

Shape factor, T, quantifies the shape of a sample's anisotropy ellipsoid:

$$T = [2\ln(K_{int} / K_{min})] / [\ln(K_{max} / K_{min})] - 1$$

If T is positive ($0 < T \le 1$), the ellipsoid is oblate, whereas if T is negative ($-1 \le T < 0$), the ellipsoid is prolate. (Tarling & Hrouda, 1993)

The K_M vs. T plot of all measured samples (Fig. 17) does not show any relationship between susceptibility and shape factor, which suggests that the variations in anisotropy are not due to variations in the concentration of ferromagnetic minerals. French (2006) and Housen (personal communication with French, 2006) suggest that the weakness of the susceptibility signal may mean that small variations in mineralogy are producing large changes in shape factor.
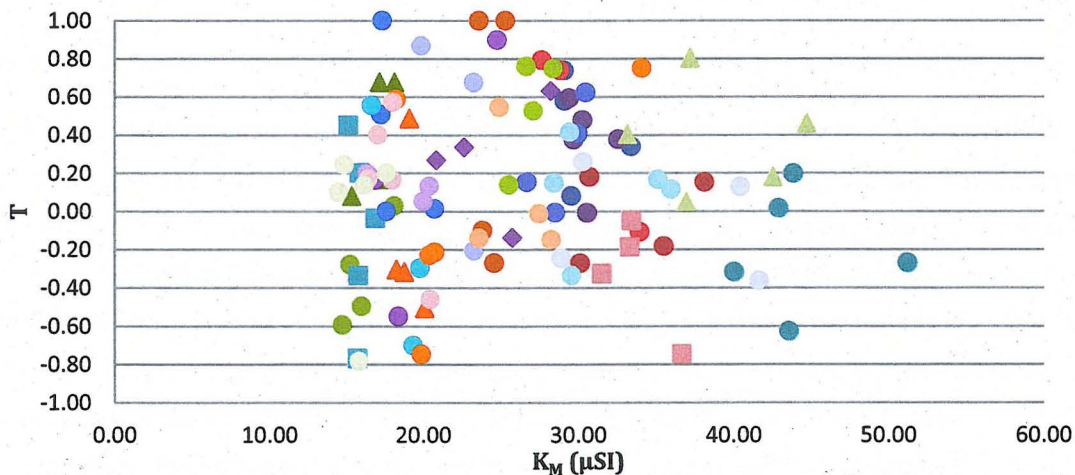
Figure 17. Shape factor, T, vs. mean susceptibility, K_M. Colored points represent different hand samples; points with the same color represent cubes from the same hand sample.

Corrected degree of anisotropy, Pj, is a measure of the magnitude of anisotropy that uses logarithmic values of all three susceptibilities:

$$Pj = \exp \sqrt{\{2[(\eta_1 - \eta_m)^2 + (\eta_2 - \eta_m)^2 + (\eta_3 - \eta_m)^2]\}}$$

where $\eta_x = \ln K_x$ and $\eta_m = \sqrt[3]{(\eta_1 \, \eta_2 \, \eta_3)}$. French (2006) used a Pj vs. T plot to determine whether flattening strains, indicated by oblate ellipsoids, or constrictional strains, indicated by prolate ellipsoids, dominate deformation at Durmid Hill. If one or the other was the case, larger values of Pj would correlate with the associated T values. Neither French's data nor the Pj vs. T plot of all measured samples from this study (Fig. 18) exhibit a distribution pattern favoring one of these options. Rather, measurements are randomly scattered, suggesting that there is no dominant maximum or minimum AMS component. (French (2006) uses the variable P' instead of Pj to represent the corrected degree of anisotropy.)
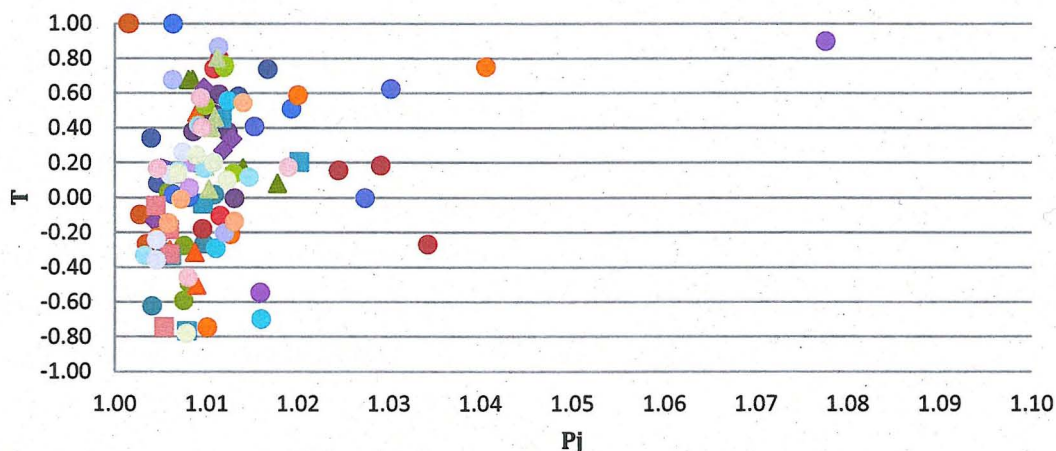
Figure 16. Shape factor, T, vs. corrected degree of anisotropy, Pj. Colored points represent different hand samples; points with the same color represent cubes from the same hand sample.

To analyze my results on an individual basis, each cube's susceptibility axes and the sample's associated bedding plane were plotted using OSXStereonet. The resulting stereonets were sorted into four categories: K_{max} perpendicular to bedding (8 samples), K_{min} perpendicular to bedding (5 samples), K_{int} perpendicular to bedding (3 samples), and samples that defied categorization due to strange orientations or a lack of sufficient data (10 samples). Most samples exhibited a substantial amount of scatter between cube axis orientations. When the stereonets were sorted by source region, no clear trends appeared. Susceptibility directions did not exhibit any relation to distance from the fault. Patterns relating susceptibility axes to bedding or known deformation features are weak, if present, and countered by the difficulty in categorizing nearly half of the samples. (See Appendix C for AMS stereonets from all measured samples.)

REMANENCE

The remanence measured in each cube after AF demagnetization was analyzed with Craig Jones'
PaleoMag 3.1 (available at http://cires.colorado.edu/people/jones.craig/PMag3.html). Maximum
angular deviations (MAD) ranged from 3.50° to 14.40°, with most cubes producing moderately
well-defined vector components with a MAD between 8° and 12°. (Results with a MAD above 10°
are often discarded but I chose to include them in this study because my intended analysis was
general and I had few results with a MAD below 10°.) Raw declinations and inclinations were
sorted by hand sample and plotted with associated bedding planes in OSXStereonet. Remanence
directions were rotated with bedding to horizontal to account for tilt.

This portion of the study was intended to
determine whether significant vertical-axis
reorientation has occurred at Durmid Hill,
which would be indicated by either a mean
remanence direction or a trend in remanence
directions that could be related to the known
original orientation of the Bishop Tuff, D =
~348°, I = ~53° (Palmer, 1996). When the tilt-
corrected remanence directions are plotted on
a single stereonet, however, no trend appears
(Fig. 19). Extremely loose clusters of
declinations are offset by inclinations ranging
from near-vertical to completely horizontal.
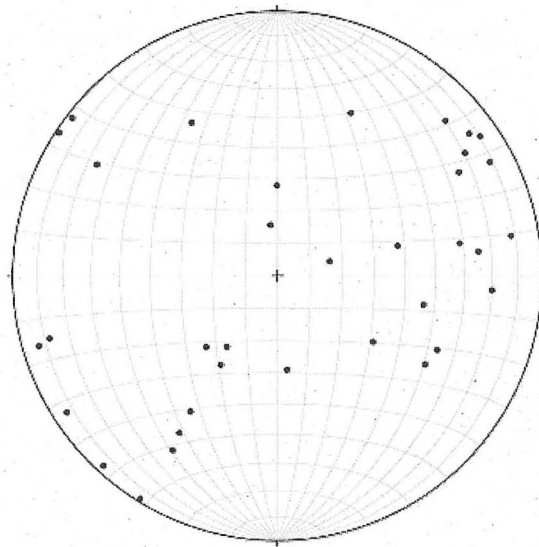
Figure 179. Tilt-corrected remanence directions of all measured
samples. Plotted with OSXStereonet.

It should be noted that even before AF demagnetization, all samples exhibited generally weak
magnetizations within two orders of magnitude of the SQUID's sensitivity. As such, there is a
chance that background noise from the instrument itself has influenced these results.

DISCUSSION

CHARACTERIZATION

The weak ferromagnetic component of the magnetic signal is accounted for by SD magnetite, which is present both within the glass and as independent grains that crystallized immediately prior to and during eruption. Hematite, another common ferromagnetic contributor, is absent.

The reported magnetic behavior may be interpreted to determine the grain size of magnetite in the Bishop Ash at Durmid Hill. First, domain state is directly dependent upon grain size; as such, the SD traits exhibited by magnetite grains in these samples provide an upper bound for their diameters. Butler (1992) cites the upper size limit for SD magnetite as 100 nm; Dunlop & Özdemir (1997) revises this figure to 50-60 nm; Witt et al. (2005) cite 65 nm (Feinberg, personal communication 2011). Second, the Verwey transition only occurs in magnetite crystals greater than 37 nm in diameter, below which the effects of superparamagnetism make detection difficult (Opdyke & Channell, 1996; Özdemir, Dunlop, & Moskowitz, 1993). Consistent observation of the Verwey transition provides a lower bound for magnetite grain diameters.

The magnetite grains in this portion of the Bishop Ash at Durmid Hill must be between 37 nm and 65 nm in diameter. This explains the difficulty French (2006) experienced when looking for ferromagnetic minerals via optical microscopy and justifies the decision to apply rock magnetic techniques to the Bishop Ash. The magnetite grains present in the Bishop Ash from this area are simply too small to be seen, even by SEM.

The dominant paramagnetic signal detected by both the VSM and the MPMS is consistent with previous work (French, 2006; Anderson, 2000) identifying feldspar and biotite in the Bishop Ash, as well as petrographic and scanning electron microscopy performed on thin sections from three samples in this study. There is no readily apparent tectonic fabric in the thin sections studied via SEM, though a sedimentary fabric is present, indicated by the modest alignment of elongate grains roughly parallel to bedding. French (2006) observed clear alignment of elongate grains and smaller fragments closer to the San Andreas Fault, but this pattern is less prominent in samples from my study area. Significant compaction has occurred in this region, as indicated by the low porosity of all three samples studied.

French (2006) found through SEM analysis that grains from one sample were Al-enriched at their rims and Al-depleted at their cores, which she proposed as evidence of extensive weathering that

resulted in leaching and recrystallization of the Bishop Ash. However, petrographic microscopy in this study reveals a thin coating around most large grains, but no clear alteration of the glass at an optically detectable scale. The Al-enriched rims might be accounted for by the coating if it is composed of illuvial clay. Alternatively, French's samples may have experienced greater alteration than those collected farther from the fault. It is also worth noting that there are numerous gypsum-filled veins in folded sedimentary layers across Durmid Hill, suggesting a high concentration of pore fluids that might account for the alteration of shard rims.

AMS AND DEFORMATION

In accordance with the results from French (2006), I anticipated that the magnetic lineations and foliations recorded by the AMS fabric from my study area might show trends relating to subsurface deformation features or distance from the San Andreas Fault. Contrary to my expectations, the AMS results have exceedingly low confidence (most do not exhibit more than 1.5% anisotropy) and do not show any readily apparent trends that could be linked to deformation. Nevertheless, several important conclusions can be drawn from these results.

The Bishop Ash at Durmid Hill has clearly experienced a significant amount of deformation, unlike the Bishop Ash in the Borrego Badlands, where the AMS results reported by Housen exhibit a high degree of order. In this region to the west of the Salton Sea, samples show high susceptibilities and well-defined anisotropy parameters with K_{min} perpendicular to bedding (Housen, personal communication with Wojtal, 2011). The low susceptibilities at Durmid Hill may have contributed to the difficulty experienced in measurement and the resulting inconsistencies.

There are multiple possible explanations for the lack of AMS trends in the Bishop Ash at Durmid Hill. The sedimentary fabric seems to be largely intact; however, some type of disruption must have occurred to reorder AMS orientations. If this area exhibited the type of continuous deformation suggested by French (2006), involving extensive fracturing and reorientation by transpressional strains, new patterns of AMS orientation should have been produced instead. The slight reordering of the sedimentary fabric may be the result of tectonic deformation just strong enough to disrupt AMS measurements, but still so weak that its results are optically undetectable. This weak tectonic fabric could even be oriented as anticipated, with a parallel strike and steeper dip than that of associated bedding. Another suggested explanation is particulate flow, whereby a small amount of reorientation of the glass shards and associated minerals would have disrupted any existing patterns. Both of these proposals would account for the lack of a strong fabric under SEM.

27

The lack of well-clustered AMS data may also be a product of the small amount of chemical alteration recorded by Anderson (2000) and French (2006). According to French's measurements, most constituents are unaltered, though small increases in iron and decreases in sodium, silica, and potassium were detected in some samples. Due to the extremely weak susceptibility of the Bishop Ash in this region, minor changes in chemistry could have caused significant disturbance of AMS patterns. The small degree of alteration measured near the fault may thereby have contributed to the observed disorder.

As glass shards were exposed to the elements after deposition, alteration may have resulted in devitrification, stripping iron and silica out of the glass to produce clay minerals. It has been suggested that these iron-bearing phyllosilicate minerals, formed as the glass altered, control the AMS of samples from Durmid Hill. Several of the samples with relatively well-defined anisotropy parameters show what appears to be a connection between bedding orientations and susceptibility orientations. In seven samples collected from sites where bedding dips southwest with a strike between 90° and 180°, K_{max} is parallel to the bedding pole. In contrast, three samples collected from sites where bedding dips southeast with a strike between 30° and 70° have K_{min} parallel to the bedding pole. This suggests that the low anisotropy in my samples might be controlled by platy clay minerals formed during alteration of the glass: if the basal planes of the clay were oriented parallel to the bedding plane, K_{min} would be parallel to its pole, whereas if the clay was perpendicular to bedding, K_{max} would be parallel to the bedding pole.

Although this explanation is tempting, it should be noted that only ten out of 26 samples follow the trend and the majority of results have very low confidence. Analysis of a much higher density of samples from one syncline-anticline system should indicate whether AMS in this area is actually controlled by clay minerals.

REMANENCE

My original intent in measuring the remanence of the Bishop Ash at Durmid Hill was to assess whether significant vertical reorientation had occurred in this area since deposition. This strategy follows the work of Lutz (2006), who successfully determined the extent of reorientation in associated bedding farther from the fault, and Gee et al. (2010), who confirmed that the Bishop Tuff is a viable source of reliable paleomagnetic information. However, my measurements do not exhibit any degree of alignment; in fact, their orientations had a smaller range before tilt correction than after.

The random distribution of ChRM orientations between 46 cubes from 12 samples has two possible explanations: either the region has undergone chaotic and extensive vertical reorientation, or the measured ChRM is not the original NRM. It is unlikely that this region has experienced enough vertical reorientation to produce a random array, nor is differential compaction a probable explanation. Thus, the measured ChRM must not be the original NRM, which was most likely a detrital remanent magnetization (DRM) acquired as the ash settled from air. Rather, remanence may have been acquired after deposition, either through alteration of this DRM or the creation of a chemical remanent magnetization (CRM). CRM results from grain growth and tends to interfere with laboratory experiments measuring field direction (Tarling & Hrouda, 1993). French (2006) suggested the presence of a CRM in accordance with observed weathering and alteration of clay minerals. This hypothesis is consistent with leaching measured by both French (2006) and Anderson (2000). Further study will be required to conclusively determine the origin of the measured ChRM.

CONCLUSIONS

The Bishop Ash at Durmid Hill exhibits a very weak susceptibility in comparison to outcrops farther away from the San Andreas Fault. This magnetic signal is dominated by contributions from paramagnetic minerals including biotite, feldspars, and the silicate glass making up the ash itself. The weak but detectable ferromagnetic component of the signal is accounted for by single-domain (SD) magnetite with a diameter of 37-65 nm.

In the area 1-3 km to the west of the San Andreas Fault, the Bishop Ash has experienced significant physical deformation at map scale. However, deformation at the scale of hand samples is neither strong nor well-behaved. While samples collected at distance and analyzed in previous studies show well-oriented AMS and remanence, those from the region between the fault trace and the Salton Sea are difficult to correlate with subsurface structures due to their apparent lack of organization.

AMS results indicate that the original fabric has been disrupted to a measurable extent, but the deformation intensity was not sufficient to produce the preferred orientation of mineral fragments necessary for clear alignment of primary axes. The small magnitude of this disruption is verified in thin section, where grains exhibit a high degree irregularity within general patterns of preferential orientation. Although there are indications of significant compaction, the sedimentary fabric is largely intact, indicating that the overprinting tectonic fabric is very weak. This behavior may be indicative of particulate flow, which would have resulted in the slight reorientation of grains, or slight tectonic deformation strong enough to disrupt AMS measurements but still weak enough to be undetectable in thin section. It is also possible that AMS is controlled by the orientations of clay minerals, produced by post-deposition alteration, with respect to bedding. Due to the weak susceptibility measured near the fault, the small degree of chemical alteration detected in previous studies may have had a disproportionately strong effect upon AMS axis orientations. As such, the intended application of AMS to the interpretation of deformed subsurface structures is not viable.

The measured characteristic remanent magnetization (ChRM) of the Bishop Ash is not its original NRM and therefore does not provide useful data on the extent of vertical axis reorientation experienced by this region. The ChRM showed a random distribution, suggesting that the measured magnetization was acquired after deposition, most likely through chemical alteration. Previous work has recognized extensive leaching and alteration of clay minerals in the Ash, consistent with the suggestion of a chemical remanent magnetization (CRM).

The results of this study do not align with anticipated trends and are therefore impossible to apply as originally intended. However, the chaos present throughout my data shows conclusively that the San Andreas Fault has measurable deformation effects not only at map scale, but also at hand-sample to microscopic scale in a region 1-3 km from the main fault trace. These effects may be related to the changing thickness of bedding layers, though they are difficult to quantify because the associated tectonic fabric is so weak.

APPENDIX A: VARIABLES

Parameter	Symbol	Units	Equation	Magnitude
Magnetization	M	Am^2/kg	Measured	
Applied field strength	H	mT	Measured	
Saturation magnetization	M_s	Am^2/kg	Measured	
Remanent magnetization	M_r	Am^2/kg	Measured	
Coercivity	H_c	mT	Measured	
Susceptibility per unit volume	K	Unitless (SI)	$K = M/H$	
Directional susceptibility	$K_{max}, K_{int}, K_{min}$	Unitless	Measured	$K_{max} \geq K_{int} \geq K_{min}$
Mean susceptibility	K_M	Unitless	$(K_{max}, K_{int}, K_{min}) / 3$	
Induced magnetization	M_i	Am^2/kg	Measured	
Mass-normalized bulk susceptibility	χ	m^3/kg	Measured	
Curie constant	C			
Shape factor	T	Unitless	$[2\ln(K_{int} / K_{min})] / [\ln(K_{max} / K_{min})] - 1$	$-1 \leq T \leq 1$
Corrected degree of anisotropy	P_j	Unitless	$\exp \sqrt{\{2[(\eta_1 - \eta_m)^2 + (\eta_2 - \eta_m)^2 + (\eta_3 - \eta_m)^2]\}}$ where $\eta_x = \ln K_x$ and $\eta_m = \sqrt[3]{(\eta_1 \eta_2 \eta_3)}$.	$1 < P_j$
Temperature	T	K	Measured	

Appendix B: Map of Sample Locations

APPENDIX C: AMS STEREONETS

KEY
■ = K_{max}
▲ = K_{int}
● = K_{min}
• = Pole to bedding plane
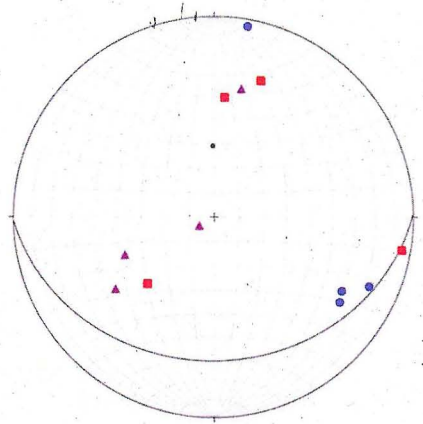
Sample Number: 07001
AMS orientation: Unknown (axis switching)
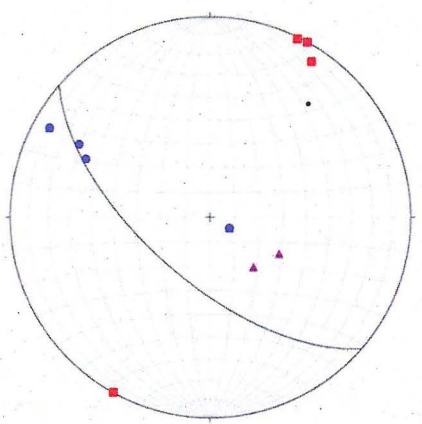
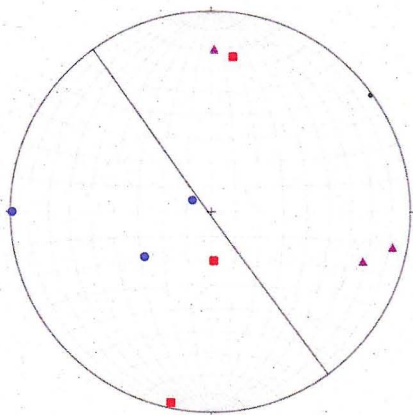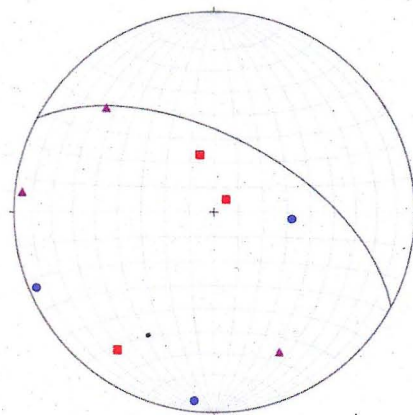*Sample Number:* 07002
AMS orientation: K_{max} perpendicular to bedding
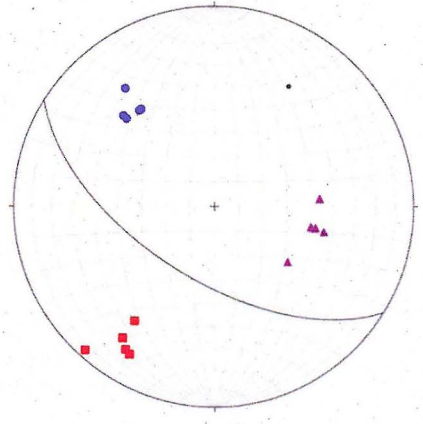
Sample Number: 07003
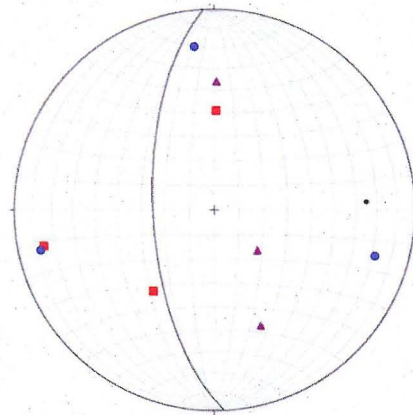*AMS orientation:* K_{max} perpendicular to bedding
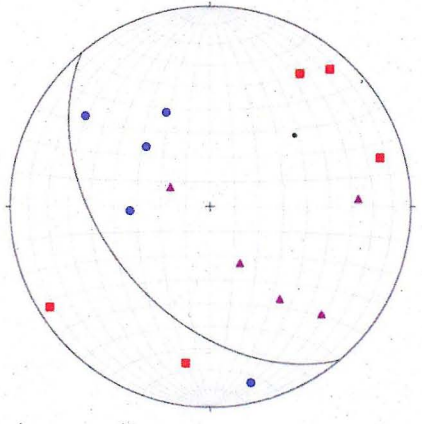
Sample Number: 07004
AMS orientation: K_{max} perpendicular to bedding
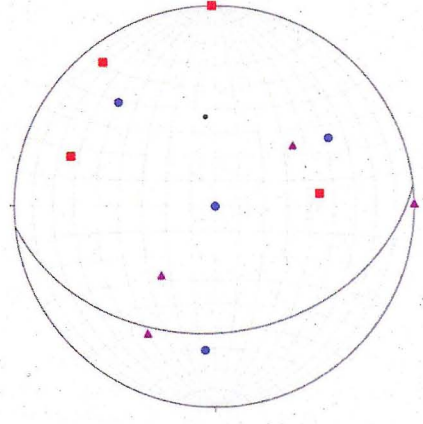
Sample Number: 07005a
AMS orientation: Unknown (axis switching)
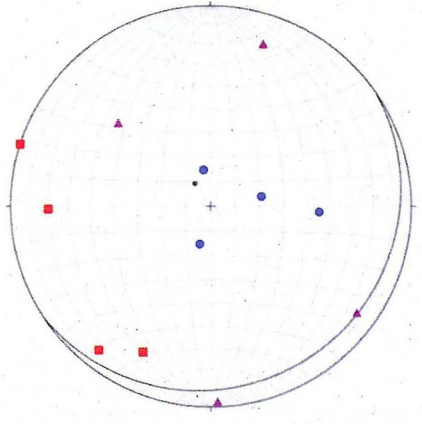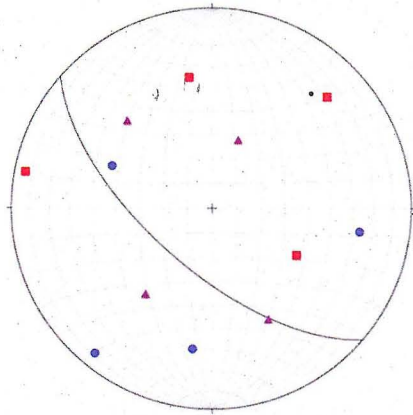

Sample Number: 07006
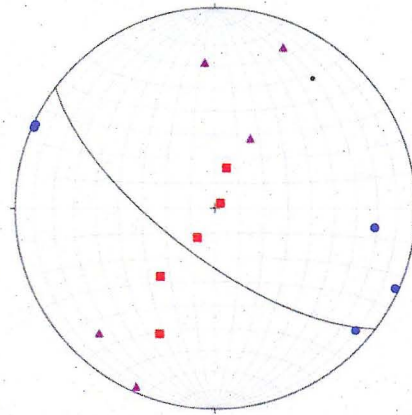*AMS orientation:* K_{min} perpendicular to bedding

34
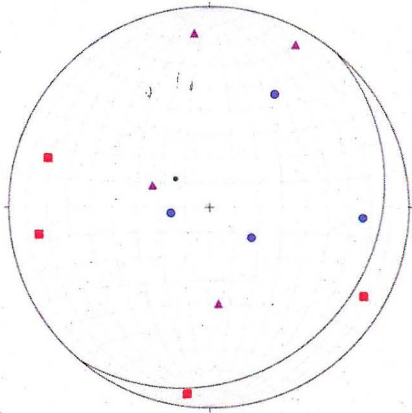
Sample Number: 07007
AMS orientation: K_{min} perpendicular to bedding
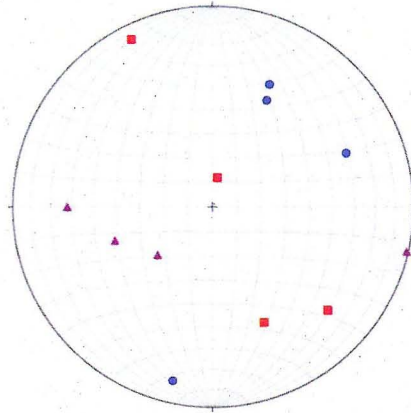
Sample Number: 07008
AMS orientation: Unknown (no bedding data)
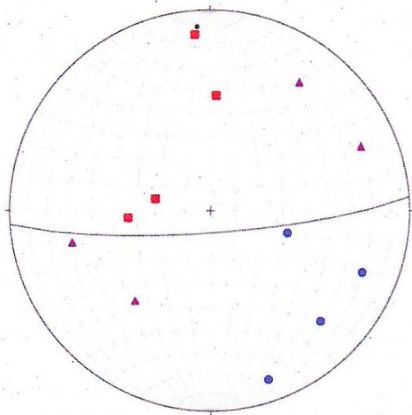
Sample Number: 07009a
AMS orientation: Unknown (scattered)
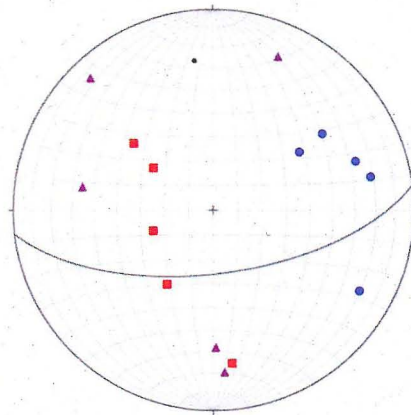
Sample Number: 07009b
AMS orientation: K_{int} perpendicular to bedding (Note skewed K_{max} great circle)
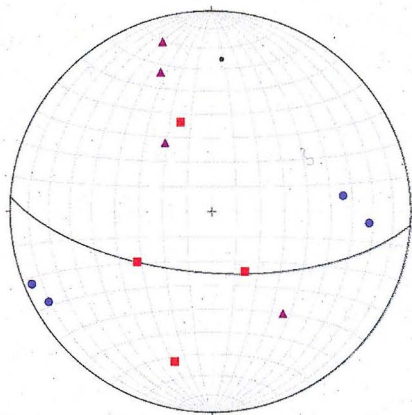
Sample Number: 07010
AMS orientation: K_{int} perpendicular to bedding
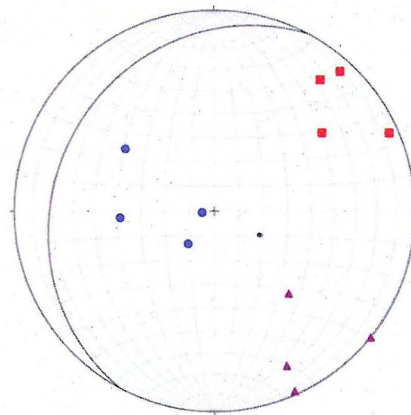
Sample Number: 07011
AMS orientation: Unknown (well-clustered, but no clear perpendicular)
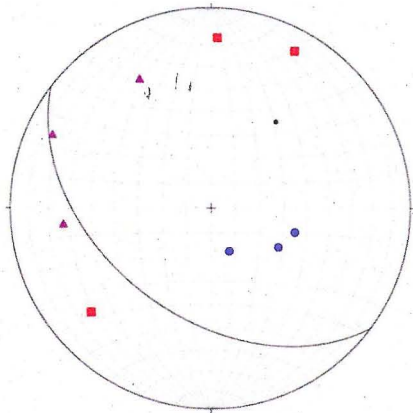
Sample Number: 07012
AMS orientation: K_{max} perpendicular to bedding
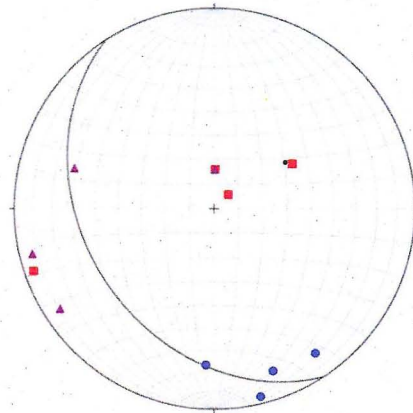
Sample Number: 07013
AMS orientation: K_{max} perpendicular to bedding

Sample Number: 07014
AMS orientation: Unknown (not enough data)

Sample Number: 07015
AMS orientation: Unknown (not enough data)
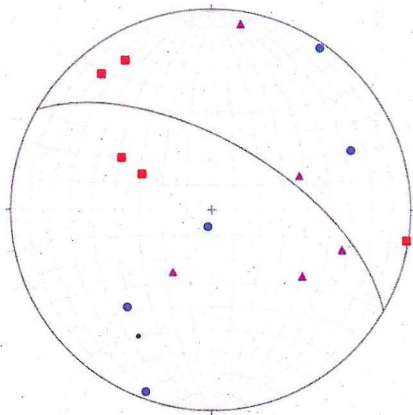
Sample Number: 07016
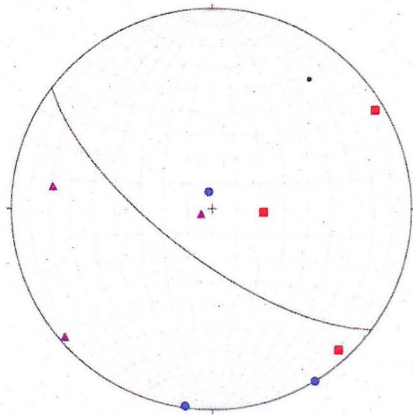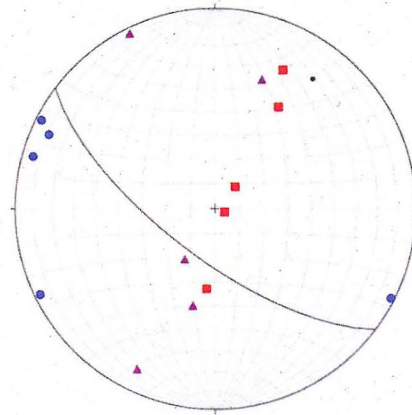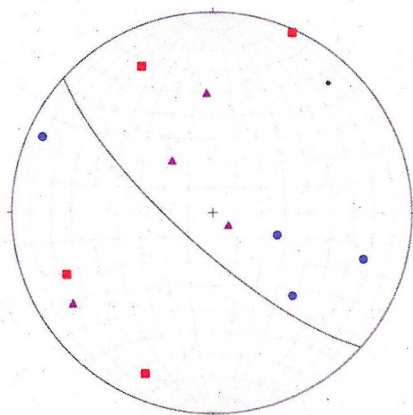*AMS orientation:* K_{min} perpendicular to bedding

Sample Number: 07017
AMS orientation: Unknown (not enough data)

Sample Number: 07018
AMS orientation: Unknown (scattered)

Sample Number: 07019
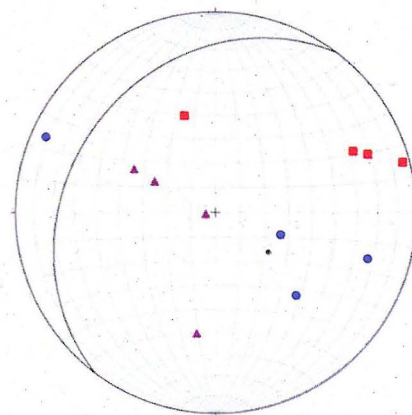*AMS orientation:* K_{int} perpendicular to bedding (Note K_{max} great circle)

Sample Number: 07020
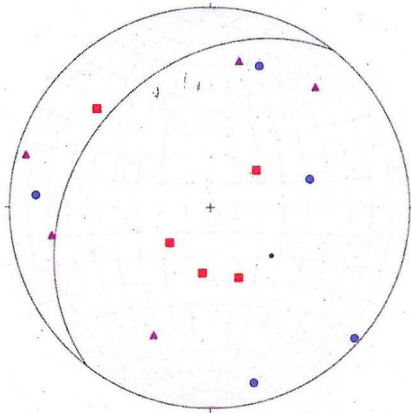*AMS orientation:* Unknown (not enough data)

Sample Number: 07021
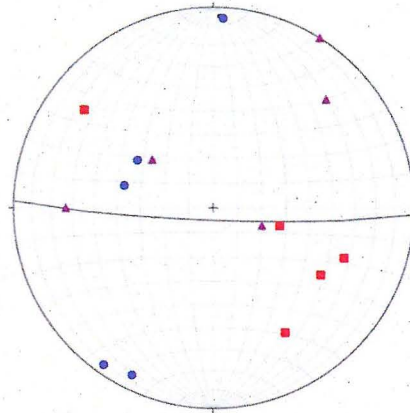*AMS orientation:* K_{max} perpendicular to bedding

Sample Number: 07022
AMS orientation: K_{max} perpendicular to bedding

Sample Number: 07023
AMS orientation: K_{min} perpendicular to bedding

Sample Number: 07024
AMS orientation: K_{max} perpendicular to bedding

Sample Number: 07025
AMS orientation: K_{min} perpendicular to bedding

ACKNOWLEDGEMENTS

REFERENCES CITED

Agnew, D.C., et al., 2002, Coseismic displacements from the Hector Mine, California, earthquake: results from survey-mode global positioning system measurements: Bulletin of the Seismological Society of America, v. 92, p. 1355-1364.

Anderson, A.T., Davis, A.M., & Fangqiong Lu, 2000, Evolution of Bishop Tuff rhyolitic magma based on melt and magnetite inclusions and zoned phenocrysts: Journal of Petrology, v. 41, p. 449-473.

Babcock, E. A., 1974, Geology of the northeast margin of the Salton Trough, Salton Sea, California: Geological Society of America Bulletin, v. 85, p. 321-332.

Borradaile, G.J., 2001, Magnetic fabrics and petrofabrics: their orientation distributions and anisotropies: Journal of Structural Geology, v. 23, p. 1581-1596.

Borradaile, G.J. & Jackson, M., 2004, Anisotropy of magnetic susceptibility (AMS): magnetic petrofabrics of deformed rocks: Geological Society of London, Special Publication, v. 238, p. 266-360.

Bowles, J., 2008, IRM gets new shielded room and u-channel magnetometer: The IRM Quarterly, v. 18, p. 1 & 7.

Bürgmann, R., 1991, Transpression along the southern San Andreas fault, Durmid Hill, California: Tectonics, v. 10, p. 1152-1163.

Butler, R.F., 1992, Paleomagnetism: Magnetic Domains to Geologic Terranes: Boston, Blackwell Scientific Publications, 319 p.

Dunlop, D.J. & Özdemir, Ö., 1997, Rock Magnetism: Fundamentals and frontiers: Cambridge, Cambridge University Press, 573 p.

French, M., Wojtal, S., & Housen, B., 2006, Transpressional deformation style & AMS fabrics adjacent to the southernmost segment of the San Andreas fault, Durmid Hill, CA: Eos Transactions of the American Geophysical Union, paper T41D-1598.

French, M., 2006, Transpression along Durmid Hill: A Record of Deformation in the Magnetic Fabric [Honors thesis]: Oberlin, Oberlin College, 64 p.

Gee, J.S., Yu, Y., & Bowles, J., 2010, Paleointensity estimates from ignimbrites: An evaluation of the Bishop Tuff: Geochemistry Geophysics Geosystems, v. 11, doi:10.1029/2009GC002834.

Gorree, W.S. & Fuller, M., 1976, Magnetometers Using RF-Driven Squids and Their Applications in Rock Magnetism and Paleomagnetism: Reviews of Geophysics and Space Physics, v. 14, p. 591-608.

Johnson, C.E. & Hutton, L.K., 1982, Aftershocks and preearthquake seismicity, U.S. Geological Survey Professional Paper, 1254, p. 59-76.

Johnson, C.E. & Hutton, L.K., 1986, A tectonic model for the Imperial Valley and its relation to seismic risk on the southern San Andreas fault (abstract), Eos Transactions of the American Geophysical Union, 67, 1200.

Jones, C.H., 2002, User-driven integrated software lives: "PaleoMag" paleomagnetics analysis on the Macintosh: Computers and Geosciences, v. 28, p. 1145-1151.

Lutz, A.T.,Dorsey, R. J., Housen, B. A., & Janecke, S. U., 2006, Stratigraphic record of Pleistocene faulting and basin evolution in the Borrego Badlands, San Jacinto zone, southern California: Geological Society of America Bulletin, v. 118, p. 1377-1397.

Merrill, R.T., McElhinny, M.W., & McFadden, P.L., 1996, The Magnetic Field of the Earth: Paleomagnetism, the Core, and the Deep Mantle: San Diego, Academic Press, 531 p.

Moores, E.M. & Twiss, R.J., 1995, Tectonics: New York, W.H. Freeman & Co., 415 p.

Opdyke, N.D. & Channell, J.E.T., 1996, Magnetic Stratigraphy: San Diego, Academic Press, 346 p.

Özdemir, Ö., Dunlop, D.J., & Moskowitz, B.M., 1993, The effect of oxidation on the Verwey transition in magnetite: Geophysical Research Letters, v. 20, p. 1671-1674.

Palmer, H.C., MacDonald, W.D., Gromme, C.D., & Ellwood, B.B., 1996, Magnetic properties and emplacement of the Bishop tuff, California: Bulletin of Volcanology, v. 58, p. 101-116.

Philibosian, B., Fumal, T., & Weldon, R., San Andreas Fault earthquake chronology and Lake Cahuilla history at Coachella, California: Bulletin of the Seismological Society of America, v. 101, p. 13-38.

Sykes, L.R. & Nishenko, S.P., 1984, Probabilities of occurrence of large plate rupturing earthquakes for the San Andreas, San Jacinto, and Imperial faults, California: Journal of Geophysical Research, v. 89, p. 5905-5927.

Sylvester, A.G., Bilham, R., Jackson, M., & Barrientos, S., 1993, Aseismic growth of Durmic Hill, southeasternmost San Andreas Fault, California: Journal of Geophysical Research, v. 98, p. 14,233-14,243.

Tarling, D.H. & Hrouda, F., 1993, The Magnetic Anisotropy of Rocks: London, Chapman & Hall, 217 p.

Tauxe, L., 2005, Lectures in Paleomagnetism: http://erda.sdsc.edu/website/MAGIC/books/Tauxe/2005

Witt, A., Fabian, K., & Bleil, U., 2005, Three-dimensional micromagnetic calculations for naturally shaped magnetite: Octahedra and magnetosomes: Earth and Planetary Science Letters, v. 233, p. 311-324.